Finite element modelling and image reconstruction for Lorentz force electrical impedance tomography

Finite element modelling and image reconstruction for Lorentz force electrical impedance tomography

Nick Polydorides

School of Engineering, Institute for Digital Communications, University of Edinburgh, UK.

E-mail: n.polydorides@ed.ac.uk

October 2017

Abstract. We propose a numerical framework to simulate the Lorentz Force Electrical Impedance Tomography (LFEIT) measurements on accurate electrode models and an image reconstruction scheme for which data on two pairs of electrodes are sufficient. The adopted finite element-based complete electrode model encompasses the electrode's geometry and contact impedance, accounting for the power losses at the contact interface. The results of our simulation study suggest that electrode modelling has a significant impact on the measurements and electrode model inaccuracies may be detrimental to the image reconstruction. For image reconstruction, we suggest an approach based on a modified J-substitution algorithm that requires LFEIT and impedance measurements on two pairs of sensors, essentially necessitating no more than three boundary electrodes. This allows for shorter acquisition times, less sonication noise during the acoustic modulation, a simpler measurement setup, and eventually a more succinct and efficient image reconstruction process.

Keywords: electrical conductivity, tomography, Lorentz force effect, current density fitting, contact impedance.

Submitted to: *Physiol. Meas.*

1. Introduction and contributions

Lorentz Force Electrical Impedance Tomography (LFEIT) [1], also known as Magneto-Acousto-Electric Tomography [2], or Ultrasonically-induced Lorentz force tomography [3], [4] has recently emerged as an alternative to Electrical Impedance Tomography (EIT) that yields, in principle, noise-robust, high-resolution, quantitative conductivity imaging, aimed in particular for breast screening. The existing literature relies predominantly on modelling the LFEIT measurements either on simplistic point electrode, assuming perfect contact with the domain to be imaged or contactless induction sensing on coils [5], [6], [7]. In this work we go beyond this state of

development to contribute a more accurate complete electrode model (CEM) for these measurements on realistic, finitely sized electrodes that dissipate some electric power, as we investigate numerically the impact of electrode modelling errors on the data and image reconstruction [8]. In this context we suggest also an image reconstruction approach that lifts the requirement of having many boundary electrodes and a homogeneous boundary conductivity profile. We note that a detailed review of the developments of the modality is outside the scope of this paper, and we refer the readers to some of the landmark papers, from its inception as a potential bio-imaging technique [9], the benchmark experiments to measure the Lorentz force induced signals in biological samples [10], [11], the choice of acoustic modulation methods [12], [4] to the more recent expositions on computational modelling, analysis and image reconstruction [3], [2] and [6] and the experimental validation of the modality [1], [5].

Its current state of development raises a number of interesting questions, including the number of electrodes and measurements necessary for image reconstruction, and what is the impact of electrode losses and modelling inaccuracies on image errors? As the signal to noise ratio can be improves either by increasing the magnetic field intensity or the pressure of the acoustic modulation as far as safety and practicality limits would allow, here we investigate explicitly how the geometry and contact impedance of the electrodes influence the measurement. Thereafter we discuss an image reconstruction strategy suitable LFEIT models that are numerically approximated using the finite element method (FEM).

2. Complete electrode modelling in LFEIT

At the quasi-static approximation limit, the time-harmonic Maxwell's equations for a closed domain $\Omega \in \Re^3$ with smooth boundary $\partial\Omega$ and bounded, isotropic conductivity $0 < \sigma < \infty$, satisfy the irrotational and solenoidal conditions

$$\nabla \times \mathbf{E} = 0, \quad \nabla \cdot \mathbf{J} = 0 \quad \text{in} \quad \Omega, \tag{1}$$

for an electric field $\mathbf{E} = -\nabla u$, current density $\mathbf{J} = \sigma\mathbf{E}$ and u the electric potential field. With $L \geq 2$ disjoint electrodes attached to the boundary, the normal component of the current density there is

$$\mathbf{J} \cdot \mathbf{n} = \begin{cases} z_\ell^{-1}(u - U_\ell) & \text{for } \Gamma_\ell \\ 0 & \text{for } \partial\Omega \setminus \cup_{\ell=1}^{L} \Gamma_\ell \end{cases}, \ \ell = 1, \ldots, L, \tag{2}$$

where $\mathbf{n}$ is the outward unit normal on $\partial\Omega$, $z_\ell > 0$ is the ℓth electrode's contact impedance value, Γ_ℓ its surface and U_ℓ the electrode potential [13]. When a Lorentz force current density $\mathbf{J}_L$ is induced by the ionic motion of the conductivity under the influence of an acoustic velocity field $\mathbf{v}(t)$ and a magnetic field $\mathbf{B}$, an Ohmic current density $\mathbf{J}_O$ is generated in response to the electric potential u created by $\mathbf{J}_L$. At any time t for which the acoustic velocity within the domain is not zero, the total current in the domain is

$$\mathbf{J}(t) = \mathbf{J}_L(t) + \mathbf{J}_O(t), \quad \text{where} \quad \mathbf{J}_L = \sigma\mathbf{B} \times \mathbf{v}(t), \quad \text{and} \quad \mathbf{J}_O = -\sigma\nabla u(t). \tag{3}$$

Since in LFEIT no currents are directly applied through the electrodes, integrating the normal component of the current density over the surface of the electrode yields

$$\int_{\Gamma_\ell} \mathrm{d}s \, \frac{1}{z_\ell}(u - U_\ell) = 0, \tag{4}$$

from where we deduce that the electrode potential at a given instant of time is simply the average of the potential's profile over the electrode,

$$U_\ell = |\Gamma_\ell|^{-1} \int_{\Gamma_\ell} \mathrm{d}s \, u, \quad \ell = 1, \ldots, L, \tag{5}$$

where the potential u depends also on the values of z_ℓ for each electrode, and $\mathrm{d}s$ represents a surface measure. The LFEIT signal M between two electrodes, say ℓ and m, is thus the time-varying potential

$$M(t) = U_\ell(t) - U_m(t), \quad t \geq 0. \tag{6}$$

Due to the reciprocity of the Green's function in the governing equation $\nabla \cdot \sigma \nabla u = 0$ the LFEIT-CEM measurement is simpler to describe in terms of the adjoint model that refers to the hypothetical potential induced when the measuring electrodes inject currents [14]. In this case, and although LFEIT does not entail boundary excitation, we consider the adjoint currents I_ℓ which yield an adjoint potential w and a corresponding current density $\mathbf{J}^a(t) = -\sigma \nabla w(t)$, related through the *adjoint* model

$$\nabla \cdot \mathbf{J}^a = 0 \quad \text{in } \Omega, \tag{7}$$

$$\mathbf{J}^a \cdot \mathbf{n} = 0 \quad \text{on } \partial\Omega \setminus \cup_{\ell=1}^{L} \Gamma_\ell, \tag{8}$$

$$\int_{\Gamma_\ell} \mathrm{d}s \, \mathbf{J}^a \cdot \mathbf{n} = I_\ell \quad \text{on } \Gamma_\ell \tag{9}$$

$$\mathbf{J}^a \cdot \mathbf{n} = \frac{1}{z_\ell}(w - W_\ell) \quad \text{on } \Gamma_\ell, \tag{10}$$

that attains a unique solution $(w, W) \in H^1(\Omega) \oplus \Re^L$ subject to the charge conservation and grounding conditions [13]

$$\sum_{\ell=1}^{L} I_\ell = 0, \quad \sum_{\ell=1}^{L} W_\ell = 0. \tag{11}$$

From the direct and adjoint LFEIT-CEM equations we can derive an analytic expression for the measurement $M(t)$. For $u, w \in C^2(\Omega)$ Green's second identity asserts that

$$\int_\Omega \mathrm{d}\mathbf{r} \, w \nabla \cdot \mathbf{J}_O = -\int_{\partial\Omega} \mathrm{d}s \, (u\mathbf{J}^a \cdot \mathbf{n} - w\mathbf{J}_O \cdot \mathbf{n}), \tag{12}$$

and since $\nabla \cdot (\mathbf{J}_O + \mathbf{J}_L) = 0$ from (1) the divergence theorem reads

$$\int_\Omega \mathrm{d}\mathbf{r} \, w \nabla \cdot \mathbf{J}_L = \int_{\partial\Omega} \mathrm{d}s \, u\mathbf{J}^a \cdot \mathbf{n} - \int_{\partial\Omega} \mathrm{d}s \, w\mathbf{J}_O \cdot \mathbf{n}, \tag{13}$$

As we show in the appendix evaluating the two surface integrals yields our definition for the LFEIT measurement under the CEM as

$$M(t) = -\int_\Omega \mathrm{d}\mathbf{r} \, \mathbf{J}_L(t) \cdot \nabla w(t) = \int_\Omega \mathrm{d}\mathbf{r} \, \mathbf{J}^a(t) \cdot (\mathbf{B} \times \mathbf{v}(t)) \tag{14}$$

When the material density ρ and the speed of sound c within the domain are approximately constant, assumptions that hold true within the breast tissue, the velocity satisfies the linearised Euler equation [15]. Then, following [2], we introduce the velocity potential φ from $\rho\mathbf{v} = \nabla\varphi$, and since $p = -\frac{\partial\varphi}{\partial t}$ for p the pressure field one arrives to the wave equation

$$\frac{\partial^2\varphi}{\partial t^2} = c^2\Delta\varphi, \tag{15}$$

where $\varphi(\mathbf{r}, t) = \mathrm{Re}\{\xi(\mathbf{r})e^{-i\omega t}\}$ satisfies $\Delta\xi + k^2\xi = 0$ for $k = \omega/c$ the wave number. Combining (14) and (15) yields the MAET-CEM measurement expression

$$M(t) = -\frac{1}{\rho}\int_\Omega \mathrm{d}\mathbf{r}\,\mathbf{B}\cdot\Big(\varphi(t)\,\nabla\times\mathbf{J}^a(t) - \nabla\times(\varphi(t)\mathbf{J}^a(t))\Big), \tag{16}$$

where the sought conductivity information is encoded into the curl of the adjoint current density vector $\mathrm{curl}\,\mathbf{J}^a = -\nabla\sigma\times\nabla w$. If $\varphi \in C^2(\Omega)$ is a smooth function with continuous support over Ω both integral terms in (16) are well defined. However, when φ is compactly supported at a focal point as in [1], [7] or a planar surface transecting Ω as in the synthetic focusing approach [16], [19]; adopted in the study, the integrand in the second term of (16) becomes singular, leaving an analytic expression for the measurement as

$$M(t) = \frac{1}{\rho}\cdot\Big(\int_\Omega \mathrm{d}\mathbf{r}\,\mathbf{B}\cdot\varphi(t)(\nabla\sigma\times\nabla w(t)) + \int_{\partial\Omega}\mathrm{d}s\,\mathbf{B}\cdot\varphi(t)\,\mathbf{J}^a(t)\times\mathbf{n}\Big), \tag{17}$$

with the potentially singular component confined within the surface integral. Practically one can filter out the contribution of the singular component in the LFEIT data by filtering the frequency components of the measurements outside the ultrasound modulation band.

3. Numerical implementation

We seek to develop a numerical approximation scheme for the solution of the LFEIT-CEM equations based on the FEM. As the measurement is defined in terms of the adjoint current density we develop our FEM formulation for the adjoint model equations (7)-(11). To resolve the curl of the current density we employ linear and quadratic bases of interpolation functions to approximate the electrical conductivity and the adjoint potential respectively. Recalling that the measurement model derived above assumes $w \in C^2(\Omega)$ and $\sigma \in \mathcal{S}$, where $\mathcal{S}$ is the set of bounded, positive, square integrable functions over Ω, then multiplying the governing equation $\nabla\cdot\mathbf{J}^a = 0$ with the test functions (y, Y), integrating by parts and substituting the boundary conditions yields the weak form of the LFEIT-CEM problem for the solution $(w, W) \in H^1(\Omega)\oplus\Re^L$ as

$$\int_\Omega \mathrm{d}\mathbf{r}\,\sigma\nabla w\cdot\nabla y + \sum_{\ell=1}^{L}\frac{1}{z_\ell}\int_{\Gamma_\ell}\mathrm{d}s\,(W_\ell - w)(Y_\ell - y) = \sum_{\ell=1}^{L} I_\ell W_\ell, \tag{18}$$

for all $(y, Y) \in H^1(\Omega)\oplus\Re^L$, and $\sigma \in \mathcal{S}$. The domain is subsequently discretised into a finite dimensional grid, encompassing k tetrahedral elements and n nodes, of

which n_v are at the vertices of the elements and the rest at the midpoints of the edges. If $\mathcal{S}_h = \{\chi_\tau : \tau = 1, \ldots, n_v\} \subset \mathcal{S}$ is a finite dimensional space of linear Lagrange interpolation functions spanning Ω then we consider a conductivity approximation as $\sigma_h(\mathbf{r}) = \sum_{\tau=1}^{n_v} \sigma_\tau \chi_\tau(\mathbf{r})$. Similarly, with $\mathcal{W}_h = \{\phi_i : i = 1, \ldots, n\} \subset H^1(\Omega)$ a basis of quadratic Lagrange interpolation functions we consider adjoint potentials of the form $w_h(\mathbf{r}) = \sum_{i=1}^{n} w_i \phi_i(\mathbf{r})$ and seek to compute $w_h \in \mathcal{W}_h$ and $W \in \Re^L$ such that

$$\int_\Omega \mathrm{d}\mathbf{r}\, \nabla w_h \cdot (\sigma_h \nabla y_h) + \sum_{\ell=1}^{L} \frac{1}{z_\ell} \int_{\Gamma_\ell} \mathrm{d}s\, (W_\ell - w_h)(Y_\ell - y_h) = \sum_{\ell=1}^{L} I_\ell W_\ell,$$

for all $Y \in \mathbb{R}^L$ and $y_h \in \mathcal{W}_h$ [17]. For a discrete model with k elements, n nodes and L boundary electrodes we write n equations in $n + L$ unknowns $\{w_1, \ldots, w_n, W_1, \ldots, W_L\}$

$$\sum_{i=1}^{n} \Big(\int_\Omega \mathrm{d}\mathbf{r} \nabla \phi_i \cdot (\sigma_h \nabla \phi_j) + \sum_{\ell=1}^{L} \frac{1}{z_\ell} \int_{\Gamma_\ell} \mathrm{d}s\, \phi_i\, \phi_j \Big) w_i - \sum_{\ell=1}^{L} \frac{1}{z_\ell} \Big(\sum_{i=1}^{n} \int_{\Gamma_\ell} \mathrm{d}s\, \phi_i \Big) W_\ell = 0,$$

for $j = 1, \ldots, n$. Using the boundary condition $W_\ell = w + z_\ell \sigma \nabla w \cdot \mathbf{n}$ and the definition of the adjoint currents we obtain another set of L equations

$$-\frac{1}{z_\ell} \sum_{i=1}^{n} w_i \int_{\Gamma_\ell} \mathrm{d}s\, \phi_i + \frac{1}{z_\ell} W_\ell \int_{\Gamma_\ell} \mathrm{d}s = I_\ell, \quad \text{for} \quad \ell = 1, \ldots, L,$$

and assemble the FEM algebraic system

$$\begin{pmatrix} S & T \\ T^\top & Q \\ 0 & 1 \end{pmatrix} \begin{pmatrix} w \\ W \end{pmatrix} = \begin{pmatrix} 0 \\ I \\ 0 \end{pmatrix}, \tag{19}$$

for $S = S^\Omega + S^\Gamma$ where the matrices S, T and Q have entries

$$S^\Omega_{i,j} = \int_\Omega \mathrm{d}\mathbf{r} \nabla \phi_i \cdot (\sigma_h \nabla \phi_j), \quad S^\Gamma_{i,j} = \sum_{\ell=1}^{L} \frac{1}{z_\ell} \int_{\Gamma_\ell} \mathrm{d}s\, \phi_i \phi_j, \quad i, j = 1, \ldots, n,$$

$$T_{i,\ell} = -\frac{1}{z_\ell} \int_{\Gamma_\ell} \mathrm{d}s\, \phi_i, \quad \text{and} \quad Q_{\ell,\ell} = \frac{1}{z_\ell} \int_{\Gamma_\ell} \mathrm{d}s, \quad i = 1, \ldots, n, \quad \ell = 1, \ldots, L.$$

where $I \in \mathbb{R}^L$ is the vector of adjoint currents that correspond to the LFEIT-CEM measurement patterns on the electrodes, while 0 and 1 are respectively zero and ones vectors that impose the uniqueness condition (11) on w and W in the least squares sense. The integrals above are evaluated numerically using Gauss quadrature rules [17] to yield a piecewise quadratic approximation for $\mathbf{J}^a$ and a piecewise linear for the corresponding $\operatorname{curl} \mathbf{J}^a$. Upon solving for w, the adjoint current density and its curl are readily available on each element and the LFEIT data are computed by integrating $\operatorname{curl} \mathbf{J}^a$ on the hyperplane of φ as it transects the domain.

4. Image reconstruction

The image reconstruction assumes that measurements have been collected in three orthogonal directions of the magnetic field $\mathbf{B}^{\boldsymbol{\eta}_1}$, $\mathbf{B}^{\boldsymbol{\eta}_2}$ and $\mathbf{B}^{\boldsymbol{\eta}_3}$, where the unit vectors $(\boldsymbol{\eta}_1, \boldsymbol{\eta}_2, \boldsymbol{\eta}_3)$ provide a reference frame for reconstructing the vector fields $\operatorname{curl}\mathbf{J}^a$ and $\mathbf{J}^a$ as we explain below. At each direction of the magnetic field we transmit a large number of planar wavefronts $\varphi_{\mathbf{k}}(t)$ emanating from many directions, where the subscript $\mathbf{k}$ denotes the corresponding wave vector. The measurements are subsequently fused with additive Gaussian noise of zero mean.

4.1. Reconstructing the curl of the adjoint current density

Following the approach of [2], for $\varphi_{\mathbf{k}}(t)$ an infinitely long plane in 3D space, moving in the direction $\mathbf{k}$, the non-singular part of the measurement in (17) take the form of 3D Radon data for $\operatorname{curl}\mathbf{J}^a$, provided that $\mathbf{k}$ spans the range $(\theta_{\text{azi}}, \theta_{\text{pol}}) \in [0, \pi] \times [0, \frac{\pi}{2}]$ in azimuthal and polar angles [18]. To reconstruct the curl from this data, the filtered back projection algorithm or the analytic formulas in [19] can be used, however this requires regular and structured grids. On the other hand, most mesh generators and FEM solvers for partial differential equations rely on unstructured meshes comprising tetrahedral elements of different size, orientation and volume. To cope with this complication, an appropriate approach would be to formulate a linear least squares problem to estimate approximately the required curl in an element-wise constant basis. Suppose $\mu = \{M(t_1), \ldots, M(t_{n_t})\}$ is a time series of n_t measurements in the direction $\boldsymbol{\eta}_1$ over a period when a particular $\varphi(t)$ was propagating through Ω. Discretising the volume integral in equation (17) in the direction $\boldsymbol{\eta}_1$ and accounting for all n_k wave directions yields an overdetermined, well-posed system

$$\boldsymbol{\mu} = \Phi_{\mathbf{k}} c, \quad \text{where} \quad \Phi_{\mathbf{k}} = [\Phi_{\mathbf{k}_1}, \ldots, \Phi_{\mathbf{k}_{n_k}}]^\top, \ \boldsymbol{\mu} = [\mu_1, \ldots, \mu_{n_k}]^\top, \tag{20}$$

and c is the approximated component of $\nabla \times \mathbf{J}^a$ aligned to $\boldsymbol{\eta}_1$, while the rows $\Phi_{\mathbf{k}_i} \in \Re^{n_t \times k}$ are weighted integrals of the area of the intersection of the plane $\varphi_{\mathbf{k}_i}(t)$ with each element in the mesh of Ω, leading to a definition for the element of this matrix as

$$\Phi_{\mathbf{k}_i}(p, q) = \frac{1}{\rho} \int_{\Omega_q} \mathrm{d}\mathbf{r} \, |\mathbf{B}^{\boldsymbol{\eta}_1}| \varphi_{\mathbf{k}_i}(t_p). \tag{21}$$

A least squares estimator of the curl component can thus be obtained by $\hat{c} = \Phi^\dagger_{\mathbf{k}} \boldsymbol{\mu}$, where $\Phi^\dagger$ is the pseudo-inverse of Φ, with an error proportional to the magnitude of the noise content in the discrete data $\boldsymbol{\mu}$. The process is then repeated for the measurements in the directions $\boldsymbol{\eta}_2$ and $\boldsymbol{\eta}_3$ to recover the remaining two components of the $\nabla \times \mathbf{J}^a$.

4.2. Reconstructing the adjoint current density

The reconstruction of the adjoint current density from its curl follows closely the approach in [2], with some necessary modifications due to the dependance of $\mathbf{J}^a$ to the CEM equations. Our contribution here is on the methodology for computing the

singular integrals involved in the reconstruction of the current density within the FEM setting, that are not addressed elsewhere. Our knowledge of the model (7)-(11) asserts that $\mathbf{J}^a$ is a smooth, continuous and at least twice differentiable vector field, of which we have some noisy samples of its curl. In the adopted finite element framework the curl field is linear on elements, but our reconstruction approach resolves it in an element-wise constant basis. One may assume that constant value to be the integral of the linear approximation over the element. According to the Helmholtz decomposition theorem, as $\mathbf{J}^a$ has continuous support over the finite domain, it can be reconstructed as a sum of a solenoidal and an irrotational field as

$$\widehat{\mathbf{J}^a} = \nabla \times \mathbf{K} - \nabla\psi, \text{ where } \mathbf{K}^{\boldsymbol{\eta}_i}(\mathbf{r}) = \int_\Omega \mathrm{d}\mathbf{r}' \, \frac{\hat{c}^{\boldsymbol{\eta}_i}(\mathbf{r}')}{4\pi|\mathbf{r}' - \mathbf{r}|}, \; i = 1, 2, 3, \tag{22}$$

and $(c^{\boldsymbol{\eta}_1}, c^{\boldsymbol{\eta}_2}, c^{\boldsymbol{\eta}_3}) \in \Re^{k\times 3}$ is the reconstructed curl. Suppose further that we seek to estimate $\widehat{\mathbf{J}^a}$ at the centroids of the mesh elements. In the discrete domain this gives

$$\mathbf{K}^{\boldsymbol{\eta}_i}(\mathbf{r}) = \sum_{j=1}^{k} \hat{c}_j^{\boldsymbol{\eta}_i} \int_{\Omega_j} \mathrm{d}\mathbf{r}' \, \frac{1}{4\pi|\mathbf{r}' - \mathbf{r}|},$$

where $c^{\boldsymbol{\eta}_i}$ taken as constant over each element, and the integral exhibits the so-called 'one-over-distance' singularity. To rectify this we use Gauss's divergence theorem to recast the singular volume integrals in terms of four regular surface integrals, one for each face of the tetrahedron alleviating the singularity for all points $\mathbf{r} \in \mathrm{int}(\Omega_j)$ [20]. Effectively, as we show in the appendices,

$$\mathbf{K}^{\boldsymbol{\eta}_i}(\mathbf{r}) = \sum_{j=1}^{k} \hat{c}_j^{\boldsymbol{\eta}_i} \sum_{i=1}^{4} \oint_{\partial\Omega_j^i} \mathrm{d}s' \, \frac{\mathbf{r}' - \mathbf{r}}{8\pi|\mathbf{r}' - \mathbf{r}|} \cdot \mathbf{n}_i, \tag{23}$$

where $\partial\Omega_j^i$ denotes the ith face of Ω_j and the surface integrals can be evaluated using standard numerical quadrature, since $\mathbf{r}$ is in the interior and $\mathbf{r}'$ are restricted to the faces of the element. The reconstruction of the curl of $\mathbf{K}$ from that of $\mathbf{J}^a$ is unique subject to the solenoidal condition $\nabla \cdot \mathbf{J}^a = 0$ which governs the adjoint model. To compute the required curl we approximate the derivatives in the curl with finite differences, and evaluate $\mathbf{K}^{\boldsymbol{\eta}_i}(\mathbf{r} + \delta\mathbf{r})$ for small perturbations $\delta\mathbf{r}$ along the three orthogonal directions in consideration.

In order to reconstruct the gradient component of $\mathbf{J}^a$, we take the divergence on both sides of the decomposition (22), leading to a Laplacian equation with CEM-derived boundary conditions

$$\nabla^2\psi \quad = 0, \quad \text{in} \quad \Omega, \tag{24}$$

$$I_\ell \quad = \int_{\Gamma_\ell} \mathrm{d}s \, \nabla\psi \cdot \mathbf{n} + \int_{\Gamma_\ell} \mathrm{d}s \, \nabla \times \mathbf{K} \cdot \mathbf{n}, \quad \text{on } \Gamma_\ell \tag{25}$$

$$\nabla\psi \cdot \mathbf{n} = -\nabla \times \mathbf{K} \cdot \mathbf{n}, \quad \text{on} \quad \partial\Omega \setminus \cup_{\ell=1}^{L} \Gamma_\ell \tag{26}$$

$$\Psi_\ell \quad = \psi + z_\ell \nabla\psi \cdot \mathbf{n}, \quad \text{on} \quad \Gamma_\ell, \tag{27}$$

and the constraint $\sum_{\ell=1}^{L} \Psi_\ell = 0$ which imposes uniqueness. Note that our methodology relies on reconstructing the curl of the adjoint current density at the boundary of the

domain, while in the setting of [2] the curl vanishes on and near the boundary by virtue of the homogeneous conductivity assumption there. The Laplacian problem (24)-(27) lends itself readily available for a FEM formulation in the context of the previous section, with a coefficients matrix evaluated as in (19) for $\sigma_h = 1$ and a load vector with entries $\int_{\Gamma_\ell} \mathrm{d}s\, \nabla \times \mathbf{K} \cdot \mathbf{n}$ or $-\int_{\partial\Omega} \mathrm{d}s\, \nabla \times \mathbf{K} \cdot \mathbf{n}\, \phi_i$, over the electrode faces and otherwise respectively. This yields an expansion of ψ in the adopted quadratic basis, from where the computation of the gradient can be directly obtained.

4.3. Reconstructing the conductivity

From the estimated $\widehat{\mathbf{J}^a} \in \Re^{k\times 3}$ the final step of the imaging process is to reconstruct the conductivity from the model $\mathbf{J}^a = -\sigma\nabla w$, a task that fits into the so-called current density impedance imaging [21], [22], from where we deduce that $\mathbf{J}^a$ or $|\mathbf{J}^a|$ resolve the conductivity up to a scaling constant. As shown in [22] the knowledge of two linearly independent currents $\mathbf{J}^{a_1}$ and $\mathbf{J}^{a_2}$ suffices to reconstruct the gradient of the logarithm of a 3D conductivity in a basis aligned to the vectors $(\mathbf{J}^{a_1}, \mathbf{J}^{a_2}, \mathbf{J}^{a_1} \times \mathbf{J}^{a_2})$, after which one can compute the conductivity image by spatial integration. A similar approach is also followed in [2], where the interior conductivity is reconstructed from its gradient through a Poisson equation with $\sigma = 1$ boundary condition. However, since we make no explicit assumptions about the boundary conductivity we choose to propose a modified J-substitution algorithm [21], suitable for vector field data $\{\mathbf{J}^{a_1}, \mathbf{J}^{a_2}\}$ instead of magnitude $\{|\mathbf{J}^{a_1}|, |\mathbf{J}^{a_2}|\}$. Exploiting the parameterisation of the conductivity image in linear interpolating bases we formulate an overdetermined least squares problem for the conductivity coefficients. Moreover, with a small overhead on the data acquisition process, we measure independently, EIT data on the LFEIT electrodes signals under known current patterns I^{a_1} and I^{a_2}, which we denote as ΔU^{a_1} and ΔU^{a_2}. In the assumed conductivity bases we evaluate the linear approximation

$$\widehat{\mathbf{J}^{a_i}}(\mathbf{r}_c) = -\sigma_h(\mathbf{r}_c)\nabla w_0^i(\mathbf{r}_c), \quad i = 1, 2, \tag{28}$$

where w_0^i is the adjoint LFEIT-CEM solution based on a prior guess σ_0 and $\mathbf{r}_c$ is the centroid of the mesh element. If $j^{a_1}, j^{a_2} \in \Re^{3k}$ are concatenated column versions of $\widehat{\mathbf{J}^{a_1}}$ and $\widehat{\mathbf{J}^{a_2}}$, taken constant on elements, we can form two linear systems, for the mth conductivity iterative estimate

$$j^{a_i} = A_{\{m,a_i\}}\sigma_\tau, \quad \text{for} \quad i \in \{1, 2\} \quad \text{and} \quad m = 1, 2, 3, \ldots, \tag{29}$$

where the sparse coefficient matrices $A_{\{m,a_i\}} \in \Re^{3k\times n_v}$ with $n_v \ll k$ have definitions as

$$A_{\{m,a_i\}} = -\chi(\mathbf{r}_c)\nabla w_m^i(\mathbf{r}_c), \tag{30}$$

where w_m^i is the adjoint solution for the measurement pattern I^{a_i} based on a conductivity estimate σ_m. Starting from an initial guess σ_0, the conductivity resolving iteration proceeds as

$$\sigma_{m+1} = \begin{cases} \kappa_m A^\dagger_{\{m,a_1\}} j^{a_1} & \text{when } m \text{ odd} \\ \kappa_m A^\dagger_{\{m,a_2\}} j^{a_2} & \text{otherwise} \end{cases}, \quad \text{for } m = 0, 1, 2, 3, \ldots, \tag{31}$$

and scaling constants $\kappa_m = \Delta U^{a_1}(\sigma_m)/\Delta U^{a_1}$ or $\kappa_m = \Delta U^{a_2}(\sigma_m)/\Delta U^{a_2}$ at odd and even iteration indices respectively, where $\Delta U^{a_1}(\sigma_m)$ is the electrode potential difference for a model σ_m computed from (7)-(11) for a current pattern I^{a_1}.

5. Numerical results and discussion

5.1. On the adjoint forward problem

To quantify the impact of electrode modelling on the LFEIT data and demonstrate the image reconstruction algorithm, we consider a simulation study involving an inhomogeneous half-ellipsoid domain bounded in $[-0.05, 0.05] \times [-0.05, 0.05] \times [0, 0.1]$ m, similar in shape and dimensions to the human breast, as shown in figure 1. Based on this geometry we develop: a finite element model with two circular electrodes of diameter $d = 12.5$ mm, discretised to 3808 tetrahedral elements, another model with 3587 elements and two electrodes of diameter $2d$, and a third model encompassing point electrodes, positioned at the centre of the finite ones [23]. In the simulations we consider an arbitrary, non-smooth conductivity function

$$\sigma^* = \begin{cases} 1.7 + \cos(30\pi \mathbf{r} \cdot \boldsymbol{\eta}_3) \sin(30\pi \mathbf{r} \cdot \boldsymbol{\eta}_2) & \text{if } \mathbf{r} \cdot \boldsymbol{\eta}_1 > -0.03\,\text{m} \\ 1 & \text{otherwise} \end{cases} \tag{32}$$

in S/m, while the medium was assumed to be acoustically homogeneous at a density of $\rho = 700$ Kg/m^3. The pressure of the wavefront was calibrated so that initially ($t = 0$) the magnitude of the acoustic potential is $|\varphi| = 10^{-3}$ for all 990 $\mathbf{k}$ wave vectors, while a homogeneous 0.3 T magnetic field magnitude was assumed at each orthogonal direction $(\boldsymbol{\eta}_1, \boldsymbol{\eta}_2, \boldsymbol{\eta}_3)$, those taken aligned to the Cartesian frame $(\boldsymbol{x}, \boldsymbol{y}, \boldsymbol{z})$.

The finite element modelling was performed with two contact impedance values at $z_{\ell_1} = 10^{-3}$ Ω/m^2 and $z_{\ell_2} = 10^{-1}$ Ω/m^2, equal on both electrodes and all three models to yield the noiseless data in figure 2, indicating that electrode geometry has a significant but local effect on the measurements. Treating the simulated data from the model with electrode diameter d as "ground truth", we observe that the magnitude of the measurement signal reduces as the electrode area increases, and that the point electrode approximation appears to overestimate the data (locally) by as much as 30%. The larger electrode size in conjunction with the electrode's contact impedance yields a power loss at the interface, hence the lower amplitude of the recorded signal. Similar conclusions can be drawn by comparing the two sets of graphs in figure 3. On the other hand, the sensitivity of the measurement to contact impedance variations remains far less by comparison. The results in figure 3 illustrate that an increase in the contact impedance from $z_{\ell_1} = 10^{-3}$ to $z_{\ell_2} = 10^{-1}$ Ω/m^2 is largely suppressed in the data with only marginal changes in the measurements, almost irrespectively of the electrode size. The graphs in figures 2 and 3 illustrate also that for the chosen conductivity the LFEIT data are not smooth. As these are essentially weighted 3D Radon transform integrals of the $\operatorname{curl} \mathbf{J} = -\nabla\sigma^* \times \nabla w$ over the hyperplanes of the support of $\varphi(t)$, despite w being smooth, $\nabla\sigma^*$ causes $\operatorname{curl} \mathbf{J}$ to be discontinuous.

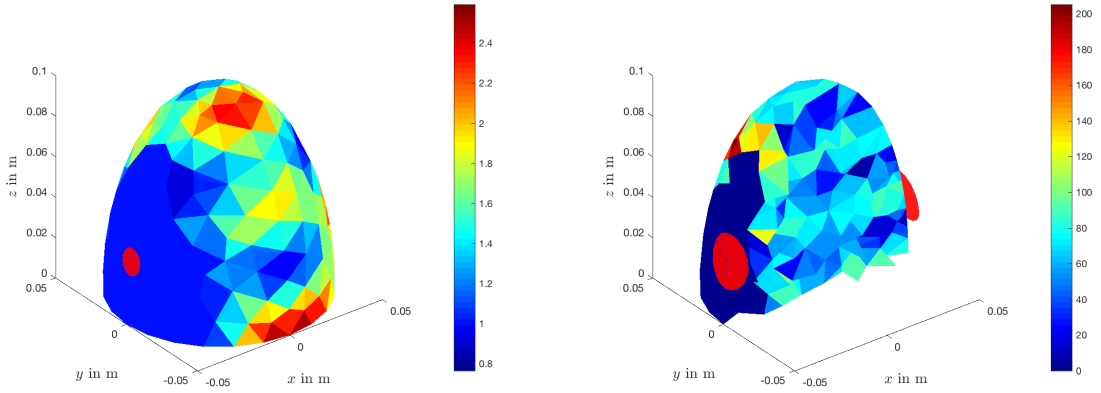

Figure 1. Left, a surface profile of the conductivity σ^* with two circular electrodes of diameter $d = 12.5$ mm, and to the right, a partial view of the magnitude of the gradient of the conductivity $|\nabla\sigma^*|$, illustrating also the two circular electrodes of diameter $2d$, centred at the same positions as the smaller ones. A third model with the same geometry and point electrodes at the centre of the circular ones is also considered in the simulation.

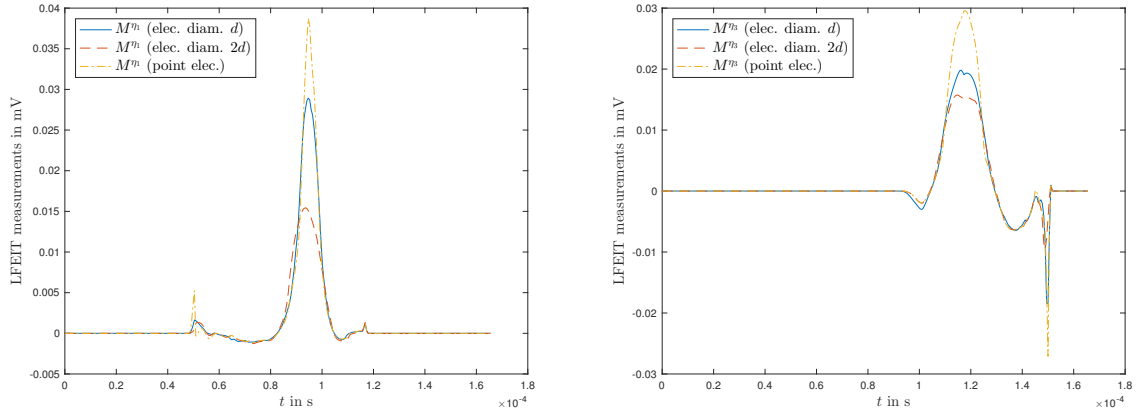

Figure 2. The effect of electrode size and shape based on a model with σ^*. Left, 500 samples of the three model measurements in magnetic field direction $\boldsymbol{\eta}_1$ and north-south acoustic field direction ($\mathbf{k}$ aligned to $\boldsymbol{\eta}_1$). Right, the measurements in the $\boldsymbol{\eta}_3$ magnetic field orientation, and $\mathbf{k}$ aligned to $\boldsymbol{\eta}_3$ in east-west direction. The discrepancies between the data waveforms affect the LFEIT signal locally with the magnitude of the measurement scaling inversely proportional with the area of the electrode surface.

5.2. On the image reconstruction problem

For image reconstruction we introduce a third electrode at the top of the ellipsoid, having the shape, size d and contact impedance z_{ℓ_1} of the other two. From these three electrodes we collect two sets of LFEIT measurements on electrode pairs, and then two EIT measurements on the same electrodes. The LFEIT measurements are then infused with a noise signal from a Gaussian distribution $\mathcal{N}(0, C)$, where $C > 0$ is a

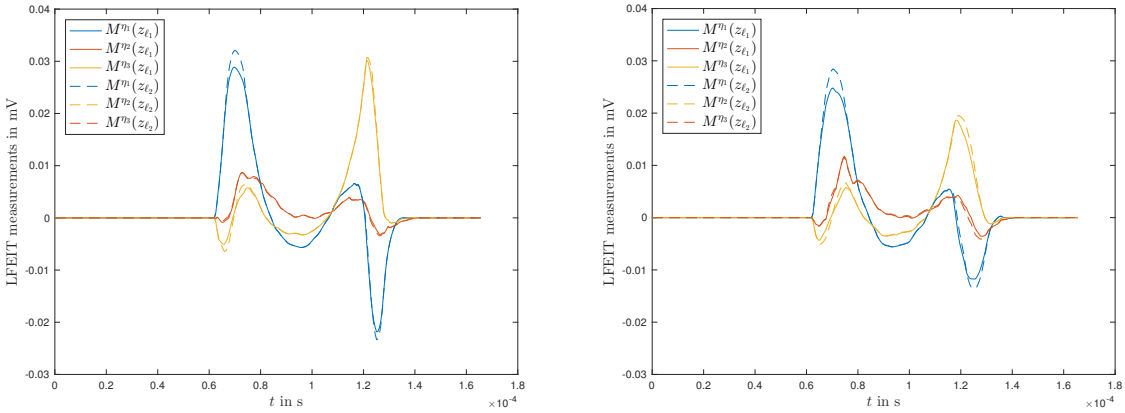

Figure 3. Effect of electrode contact impedance based on a model with σ^*. Left, the model measurements for electrode of diameter d and $z_{\ell_1} = 10^{-3}\,\Omega/\mathrm{m}$ (solid lines) and $z_{\ell_2} = 10^{-1}\,\Omega/\mathrm{m}^2$ (dashed lines). Measurements in all magnetic field orientations are illustrated for an arbitrary acoustic wave direction $\mathbf{k} = -(0.66\boldsymbol{\eta}_1 + 0.20\boldsymbol{\eta}_2 + 0.72\boldsymbol{\eta}_3)$. To the right the equivalent data for the model with electrode diameter $2d$.

positive diagonal matrix whose ith element is set $C_i = 0.05|M(t_i)|$ for $i = 1, \ldots, 500$, where $|M(t)|$ is the magnitude of the exact measurement. Reconstructing the image of the conductivity in (32) using the same model based on which the measurements were calculated, i.e. without any electrode modelling errors, the algorithm in (31) converged to a solution after 8 iterations starting from a homogenous profile guess, and the relative error in the reconstructed conductivity was found at 3%, as shown at the convergence graph at the top left of the figure 4. To reconstruct the curl of the current density from the noisy LFEIT data we have simulated a total of 990 $\mathbf{k}$ wavevectors for each orthogonal magnetic field direction, yielding 500 measurement samples per $\mathbf{k}$ direction. Based on the nonzero section of the resulting M data, we have assembled the algebraic system in (20) leading to a least squares problem with 22100 equations in 3808 curl coefficients. The relative error in the reconstructed curl was at found at 6%, however, we observed that this grows higher when using fewer directions (angles) and a coarser time discretisation.

In repeating the image reconstruction process using the measurements computed above from the model with electrode diameter d as a "ground truth", but running the image reconstruction process using the point electrode model for the same levels of additive noise, led to a significantly compromised performance, with the algorithm ending abruptly at 80% relative error. However, to mitigate the data discrepancies due to electrode modelling errors we modify the target conductivity $\sigma^* \to \tilde{\sigma}$ so that it attains a constant value within a thin layer near the boundary. This modified target yields LFEIT-CEM data with relative discrepancies between the d diameter and point electrode models that are about 6% in norm. Repeating the computations with the point electrode model and additive Gaussian noise at the previous levels, the image reconstruction algorithm started to converge after 5 iterations as shown at the top right

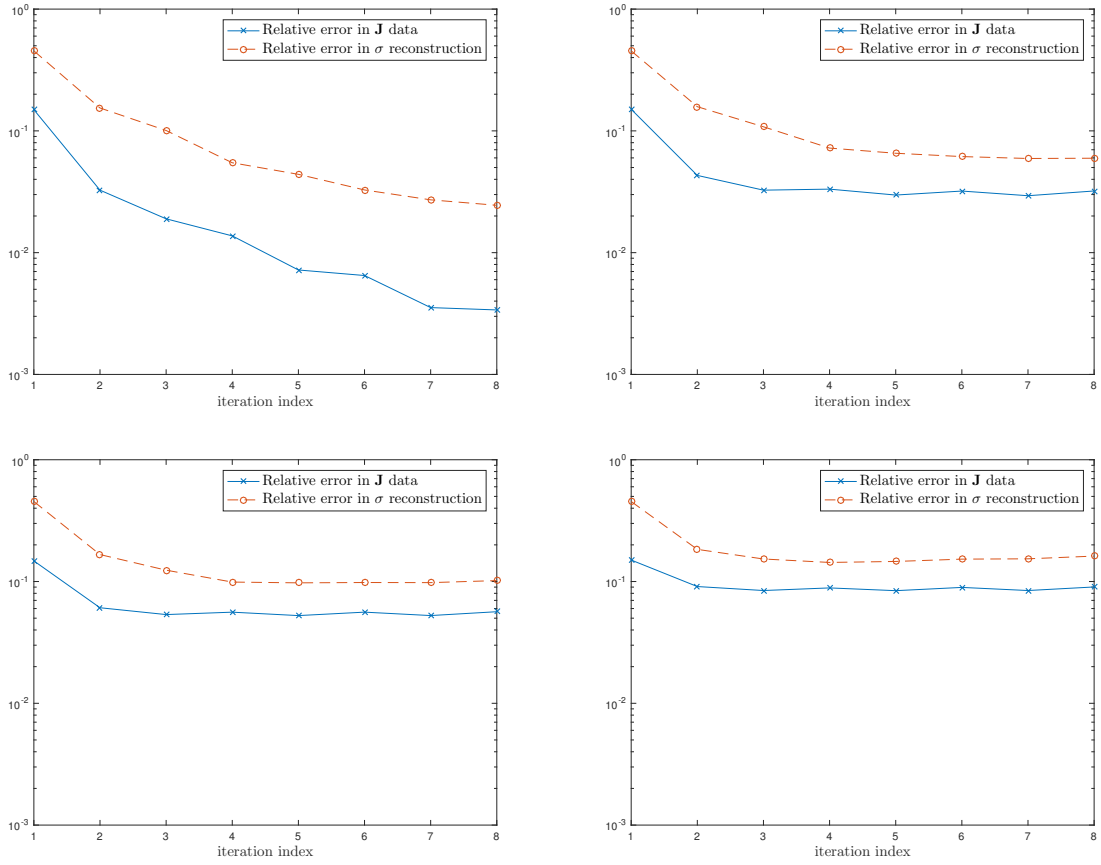

Figure 4. Convergence of the modified J-substitution-based scheme in (31). At the top left the case with no electrode modelling errors, and LFEIT measurements contaminated with zero mean Gaussian noise, and to its right, the corresponding convergence curve with fitting based on a different electrode model, but with a thin uniform conductivity layer at the boundary. At the bottom row, the convergence when additive noise levels where raised from 5%, to 7% (left) and 10% (right) respectively.

plot of figure 4, and algorithm was terminated at the eighth iteration to a relative data misfit error of about 6%, yielding the reconstructed images illustrated in figure 5. Despite the good resemblance between the target and reconstructed images, the relative conductivity reconstruction error was computed at about 10%, significantly higher than the case with no electrode modelling errors. This is in agreement with the good results obtained by non-contact measurements in [5] and [7].

6. Conclusions

We present a FEM-based framework for simulation and image reconstruction in LFEIT, using the complete electrode model that is suitable to measurements on realistic electrodes with finite size and lossy contacts. This model was used to analyse the sensitivity of the LFEIT measurements to the electrode characteristics, with our simulation suggesting that the electrode interface area has a bigger impact than its

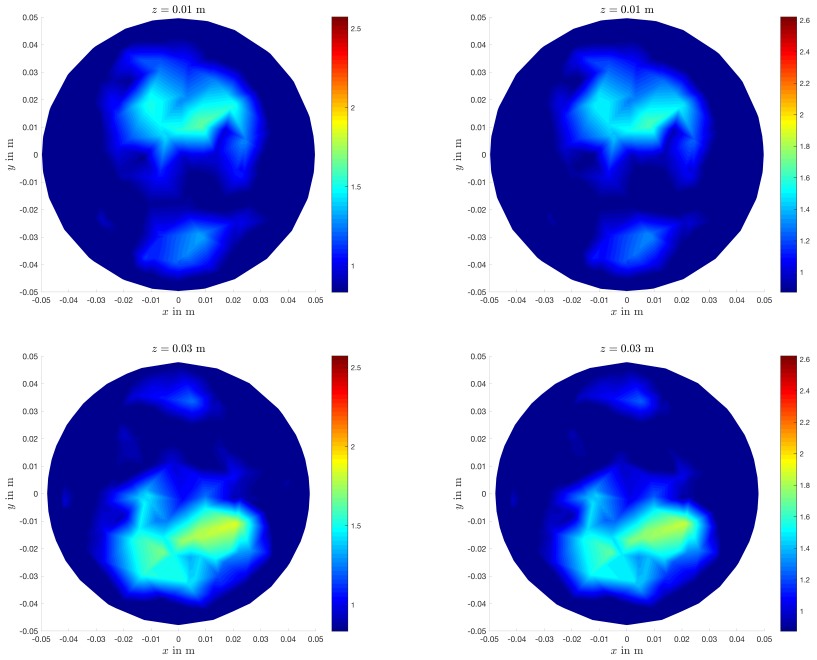

Figure 5. To the left, parallel parallel cross sections of the targeted conductivity $\tilde{\sigma}$, and to the right the corresponding sections from the image reconstruction. Notice that the good quality in the spatial resolution is due to the uniform conductivity near the three electrodes, which suppresses the electrode-modelling imperfections.

contact impedance, while showing that electrode modelling errors become negligible in domains with homogeneous boundary conductivity. For image reconstruction we suggest a modification on Kunyansky's approach [2] that is appropriate to the adopted numerical framework, and can yield images using LFEIT and EIT measurements only on two pairs of electrodes. This approach to the inverse problem, which includes a modified version of the J-substitution algorithm was found to be robust to measurement and electrode modelling error, when the conductivity in the vicinity of the measuring electrodes has small or zero gradient.

Appendix A. Proof of the CEM-LFEIT measurement model

Let the surface integrals in (14) be expressed as

$$S_1 = \int_{\partial\Omega} \mathrm{d}s\, u\mathbf{J}^a \cdot \mathbf{n}, \quad \text{and} \quad S_2 = -\int_{\partial\Omega} \mathrm{d}s\, w\mathbf{J}_O \cdot \mathbf{n}.$$

Expanding the surface integral S_1, considering separately the electrode surfaces and the inter-electrode gap yields

$$S_1 = \sum_{\ell=1}^{L} \int_{\Gamma_\ell} \mathrm{d}s\, u\mathbf{J}^a \cdot \mathbf{n} + \int_{\partial\Omega\setminus\cup_{\ell=1}^{L}\Gamma_\ell} \mathrm{d}s\; u\mathbf{J}^a \cdot \mathbf{n} = \sum_{\ell=1}^{L} \int_{\Gamma_\ell} \mathrm{d}s\; u\mathbf{J}^a \cdot \mathbf{n},$$

as $\mathbf{J}^a \cdot \mathbf{n}$ is zero everywhere on the boundary apart from the electrodes. Substituting $u = U_\ell + z_\ell \mathbf{J} \cdot \mathbf{n}$ from the *direct* model we obtain

$$\begin{aligned} S_1 &= \sum_{\ell=1}^{L} \int_{\Gamma_\ell} \mathrm{d}s \; u\mathbf{J}^a \cdot \mathbf{n} = \sum_{\ell=1}^{L} \int_{\Gamma_\ell} \mathrm{d}s \; (U_\ell + z_\ell \mathbf{J} \cdot \mathbf{n})\mathbf{J}^a \cdot \mathbf{n} \\ &= \sum_{\ell=1}^{L} U_\ell \int_{\Gamma_\ell} \mathrm{d}s \, \mathbf{J}^a \cdot \mathbf{n} + \sum_{\ell=1}^{L} z_\ell \int_{\Gamma_\ell} \mathrm{d}s \, (\mathbf{J} \cdot \mathbf{n}) \, (\mathbf{J}^a \cdot \mathbf{n}) \end{aligned}$$

Noticing that the first integral in the last equation is equal to the adjoint currents I_ℓ then importing the definition of the measurement M we have

$$S_1 = M + \sum_{\ell=1}^{L} z_\ell \int_{\Gamma_\ell} \mathrm{d}s (u - U_\ell) \, (\mathbf{J}^a \cdot \mathbf{n}).$$

Similarly, splitting the surface integral over $\bigcup_{\ell=1}^{L} \Gamma_\ell$ and the rest of the boundary, and then introducing the impedance boundary condition, yields

$$S_2 = \int_{\partial\Omega} \mathrm{d}s \, w\mathbf{J}_L \cdot \mathbf{n} - \sum_{\ell=1}^{L} \frac{1}{z_\ell} \int_{\Gamma_\ell} \mathrm{d}s \, w(u - U_\ell).$$

Through the divergence theorem, the volume integral in (13) becomes

$$\int_\Omega \mathrm{d}\mathbf{r} \, w \nabla \cdot \mathbf{J}_L = \int_{\partial\Omega} \mathrm{d}s \, w\mathbf{J}_L \cdot \mathbf{n} - \int_\Omega \mathrm{d}\mathbf{r}\mathbf{J}_L \cdot \nabla w,$$

and the first integral term on the right cancels out with the first integral in S_2, hence (13) becomes

$$-\int_\Omega \mathrm{d}\mathbf{r} \, \mathbf{J}_L \cdot \nabla w = M + \sum_{\ell=1}^{L} \int_{\Gamma_\ell} \mathrm{d}s \, (u - U_\ell)(\mathbf{J}^a \cdot \mathbf{n}) - \sum_{\ell=1}^{L} \frac{1}{z_\ell} \int_{\Gamma_\ell} \mathrm{d}s \, w(u - U_\ell),$$

and the two sums above can be shown to vanish. In particular, grouping them together and appealing to the boundary condition for $\mathbf{J}^a \cdot \mathbf{n}$ over $\bigcup_{\ell=1}^{L} \Gamma_\ell$ we get

$$\begin{aligned} \sum_{\ell=1}^{L} \int_{\Gamma_\ell} \mathrm{d}s \, (u - U_\ell)(\mathbf{J}_I \cdot \mathbf{n} - \frac{1}{z_\ell} w) &= \sum_{\ell=1}^{L} \int_{\Gamma_\ell} \mathrm{d}s \, (u - U_\ell)(-\frac{1}{z_\ell} W_\ell) \\ &= \sum_{\ell=1}^{L} \frac{W_\ell}{z_\ell} \Big(\int_{\Gamma_\ell} \mathrm{d}s \, U_\ell - \int_{\Gamma_\ell} \mathrm{d}s \, u \Big) = 0, \end{aligned}$$

and the last equality is due to the definition of the electrode potential (5). Substituting for S_1 and S_2 in (13) yields the definition of $M(t)$.

Appendix B. Singular integral regularisation

For a continuous, twice differentiable vector field $\mathbf{F}$ supported in a *closed* domain Ω, Gauss' divergence theorem asserts that the flux of the vector field (outward) the

boundary is equal to the volume integral of the divergence of the field

$$\int_\Omega \mathrm{d}\mathbf{r}\,\mathrm{div}\,\mathbf{F} = \oint_{\partial S} \mathrm{d}s\,\mathbf{F}\cdot\mathbf{n},$$

on which we rely to express the singular volume integrals in (22) into sums of regular surface integrals as in (23). It thus remains to express the scalar singular integral we seek to evaluate into a divergence of some smooth vector field $\mathbf{F}$

$$\int_\Omega \mathrm{d}\mathbf{r}'\,\frac{1}{4\pi|\delta\mathbf{r}|} = \int_\Omega \mathrm{d}\mathbf{r}'\;\mathrm{div}\,'\mathbf{F}(\delta\mathbf{r}),$$

where the integration and the divergence are with respect to the primed coordinates, and $\delta\mathbf{r} = \mathbf{r}' - \mathbf{r}$. To prove the surface integral in (23) we need to show that $\mathbf{F} = \frac{1}{8\pi|\delta\mathbf{r}|}\delta\mathbf{r}$. Following the approach in [20] (eq. (3)), let a scalar test function

$$g(|\delta\mathbf{r}|) = \frac{1}{4\pi|\delta\mathbf{r}|} = \mathrm{div}\,\mathbf{F}(\delta\mathbf{r}),$$

then

$$\mathbf{F}(\delta\mathbf{r}) = \delta\mathbf{r}\int_0^1 \mathrm{d}t\,t^2\,g(t|\delta\mathbf{r}|) = \delta\mathbf{r}\int_0^1 \mathrm{d}t\,t\,g(|\delta\mathbf{r}|) = \frac{1}{8\pi|\delta\mathbf{r}|}\delta\mathbf{r},$$

which can easily be verified by computing its divergence.

Appendix C. Acknowledgements

I am indebted to Leonid Kunyansky and Pol Grasland Mongrain for the many discussions on LFEIT/MAET experiments and algorithms.

References

[1] Grasland-Mongrain P, Mari J M, Chapelon J Y and Lafon C 2013 Lorentz force electrical impedance tomography, *Res. Imag. Health Tech.*, **13**(4-5), 357-360.

[2] Kunyansky L 2012 A mathematical model and inversion procedure for magneto-acousto-electric tomography, *Inv. Prob.*, **28**, 035002.

[3] Ammari H, Grasland-Mongrain P, Millien P, Seppecher L, and Seo J K 2014 A mathematical and numerical framework for ultrasonically-induced Lorentz force electrical impedance tomography, *Jour. de Math. Pur. et App.*, 1390-1409.

[4] Roth B J and Schalte K 2009 Ultrasonically-induced Lorentz force tomography, *Med. Biol. Eng. Comput.*, **47**, 573-77.

[5] Guo L, Liu G and Xia H 2015 Magneto-acousto-electrical tomography with magnetic induction for conductivity reconstruction, *IEEE Trans. Biomed. Imag.*, **62**(9), 2114-24.

[6] Ghalichi E and Gençer N G 2017 Theoretical limits to sensitivity and resolution in magneto-acousto-electrical tomography, *Phys. Med. Biol.* **62** 8025-40.

[7] Zengin R and Gençer N G 2016 Lorentz force electrical impedance tomography using magnetic field measurements, *Phys. Med. Biol.* **61**, 5887.

[8] Boyle A and Adler A 2011 The impact of electrode area, contact impedance and boundary shape on EIT images, *Physiol. Meas.*, **32**, 745-54.

[9] Wen H, Shah J and Balaban R S 1998 Hall effect Imaging, *IEEE Trans. Biomed. Eng.*, **45**(1), 119-24.

[10] Montalibet A, Jossinet J, Matias A and Cathinol D 2001 Electric current generated by ultrasonically induced Lorentz force in biological media, *Med. & Biol. Eng. & Comp.*, **39**, 15-20.

[11] Montalibet A, Jossinet J and Matias A 2001 Scanning electric conductivity gradients with ultrasonically-induced Lorentz force in biological media, *Ultras. Imag.*, **23**, 117-32.

[12] Haider S, Hrbek A and Xu Y 2008 Magneto-acousto-electrical tomography: a potential method for imaging current density and electrical impedance, *Physiol. Meas.*, **29**, 41-50.

[13] Somersalo E, Cheney M and Isaacson D 1992 Existence and uniqueness for electrode models for electric current computed tomography, *SIAM Appl. Math.*, **52**(4), 1023-40.

[14] Vauhkonen P, Vauhkonen M, Savolainen T and Kaipio J P, 1999, Three-dimensional electrical impedance tomography based on the complete electrode model, *IEEE Trans. Biomed. Eng.*, **46**(9), 1150-60.

[15] Colton D and Kress R 2013 *Inverse acoustic and electromagnetic scattering theory*, (Springer).

[16] Kuchment P and Kunyansky L 2010 Synthetic focusing in ultrasound-modulated tomography, *Inv. Prob. and Imag.*, **4**, 665-73.

[17] Jin J 2002 *The finite element method in electromagnetics* (IEEE Press).

[18] Kuchment P 2014 *The Radon Transform and Medical Imaging* (SIAM).

[19] Kunyansky L 2007 Explicit inversion formulae for the spherical mean Radon transform, *Inv. Prob.*, **23**, 373-83.

[20] Knockaert L 2011 On the analytic calculation of multiple integrals in electromagnetics, *IEEE Conf. Electromag. Adv. Appl. (ICEAA)*, 595-598.

[21] Khang H S, Lee B I, Oh S H, Woo E J, Lee S Y, Cho H M, Kwon O, Yoon J R and Seo J K 2002 J-substitution algorithm in magnetic resonance electrical impedance tomography (MREIT): phantom experiments for static resistivity images, *IEEE Trans. Med. Imag.*, **21**(6), 695-702.

[22] Hasanov K F, Ma A W, Nachman A I, Joy L M G 2008 Current density impedance imaging, *IEEE Trans. Med. Imag.*, **27**(9), 1301-9.

[23] Hanke M, Harrach B and Hyvonen N 2011 Justification of point electrode models in electrical impedance tomography,*Math. Meth. Mod. Appl. Sci.*, **21**(6), 1395-1413.